fire

MDPI

Article

Performance Comparison of Solid Walls and Porous Fences in Protecting Structures from Firebrand Attack

Ahmad Sharifian

School of Engineering, University of Southern Queensland, Toowoomba, QLD 4300, Australia; sharifia@usq.edu.au

Abstract: In bushfire-prone regions, solid walls and porous fences are commonly employed as mitigation measures against windblown embers (firebrands). This computational study evaluates and compares the performance of a 2 m high solid wall and a 2 m porous fence (38% porosity) in protecting structures from firebrand showers. Using a numerical model subjected to free-stream velocities of up to 50 m/s, flow patterns and firebrand trajectories were analyzed. The findings indicate that impermeable walls offer superior protection for immediately adjacent structures by deflecting the incident flow upwards, creating a "jump board" effect. However, the deflected flow subsequently reattaches to the ground at a downstream distance, rendering structures further downwind vulnerable to ember attack. The porous fence also exhibits a similar, albeit less pronounced, upward deflection. The simulations reveal minimal flow descent downstream of the fence at lower free-stream velocities, suggesting extended downwind protection. In the immediate downstream vicinity of the porous fence, penetration by small firebrands is possible; however, prior studies have shown that the likelihood of ignition from these embers is minimal and decreases rapidly within a short downstream distance of several metres.

Keywords: metal mesh fence; ember attack; firebrand movement; flow path; porosity; solid wall; porous fence; impermeable walls; permeable fences

Academic Editor: Hugo Rodrigues

Received: 9 January 2025
Revised: 27 January 2025
Accepted: 7 February 2025
Published: 21 February 2025

Citation: Sharifian, A. Performance Comparison of Solid Walls and Porous Fences in Protecting Structures from Firebrand Attack. *Fire* **2025**, *8*, 88. https://doi.org/10.3390/fire8030088

1. Introduction

Wildfire mitigation and control standards, such as AS 3959:2018 [1] and ASTM-2016 [2], commonly prescribe buffer zones of several hundred metres (dependent on the terrain slope between structures and vegetation) to protect assets and human life in fire-prone areas. While these spatial separation distances offer some protection, they do not eliminate the risk of firebrand ignition and secondary spot fires, as wind-driven embers can be transported over considerable distances—of the order of 30–40 km—as observed during the 2009 Black Saturday bushfires in Australia [3–8]. Expanding buffer zones to achieve complete protection is often impractical due to land-use constraints. Furthermore, near-ground firebrand transport plays a crucial role in accelerating fire propagation and endangering structures at the wildland–urban interface (WUI) [9].

Consequently, physical barriers constructed from non-combustible materials are frequently implemented to enhance structural resilience. Two primary barrier types are commonly employed: impermeable walls (zero porosity) and permeable fences. Impermeable walls effectively block firebrand penetration and induce some firebrand accumulation on their windward side [9] but exhibit relatively high drag coefficients at elevated wind speeds and obstruct visibility, which can be undesirable in certain contexts. Conversely, permeable fences experience reduced drag forces [10–36] and maintain visual permeability, facilitating

easier installation and greater aesthetic acceptance. Furthermore, reports and standard recommendations for using metal mesh to protect gutters and building openings suggest their effectiveness in mitigating ember intrusion [1]. The standard also acknowledges that the use of permeable fences may reduce building exposure to firebrand attacks [1].

However, existing research indicates that while permeable fences can impede the passage of larger firebrands, smaller firebrands can penetrate the mesh [37–42]. The size of these transmitted embers is dependent on the mesh aperture size and porosity. Studies suggest that apertures of less than 2 mm result in transmitted firebrands posing a minimal ignition risk [40,41]. Additionally, the inter-wire spacing can induce venturi effects, creating low-pressure zones between the wires, potentially generating vortices and reverse flows downstream of the mesh [40,41]. These flow structures can create low-pressure wake regions downstream of the wires [10,43–47], where some small embers become trapped, promoting their extinction [40,41]. These trapped embers, particularly after traversing a short downstream buffer zone of a few metres, are highly unlikely to ignite surrounding materials [40,41], as the glowing surface area and number density of glowing or flaming firebrands are important parameters in determining fuel bed ignition [48].

The preceding discussion highlights that both impermeable walls and permeable fences can effectively mitigate firebrand attack. However, a crucial consideration often overlooked is the potential for impermeable walls to deflect the incident flow upwards, creating a "jump" effect that can loft embers over the wall. This flow deflection phenomenon suggests that the protective capacity of impermeable walls may be overestimated in some analyses. Moreover, there is a lack of research establishing appropriate barrier heights relative to the height of the protected structures.

This study is a preliminary step in addressing this research gap by computationally investigating these phenomena. The investigation aims to determine the relative effectiveness of these protective measures under different wind speeds and to elucidate the underlying physical mechanisms governing their performance. Using computational fluid dynamics (CFD), the performance of an impermeable wall and a porous fence (38% porosity, among the lowest commercially available) is compared on a smooth, horizontal ground plane devoid of vegetation both upstream and downstream. This low porosity was chosen to maximize flow blockage, similar to a solid wall. Therefore, if this mesh demonstrates effective filtration, higher-porosity fences are anticipated to perform even better. The simulations assume that firebrand trajectories approximate flow streamlines. Research has shown that the coupled fire–atmosphere dynamics significantly influence firebrand trajectories and deposition patterns. Firebrand flight characteristics, particularly transport distance, are also dependent on particle morphology; for example, disc-shaped embers typically exhibit greater travel distances than cylindrical embers [49]. While the assumption of firebrand motion conforming to flow streamlines is a simplification, particularly for larger embers with significant inertia and aerodynamic lift/drag characteristics, it is expected to provide a valuable comparative assessment of the relative performance of solid walls and porous fences under idealized conditions.

2. Methodology

2.1. Geometric Model, Assumptions, and Boundary Conditions

Modelling a 2 m high solid wall and a 2 m high permeable fence presents significant computational challenges due to the required domain size and mesh refinement. For example, simulating a 2 m high, 20 m long permeable fence with a 2 mm aperture using a three-dimensional (3D) mesh would necessitate an impractically large number of computational cells, of the order of trillions of elements. Therefore, simplifying assumptions were necessary to reduce computational demands without compromising the key

objectives. This study employed a two-dimensional (2D) modelling approach to mitigate computational resource and time constraints.

The selected metal mesh, characterized by a low porosity, has an aperture of 1.31 mm and a wire diameter of 0.81 mm, yielding a porosity of 38% and a unit cell size of 2.12 mm. For the 2D simulations, a cross-section of the fence, taken through the centre of the unit cell and parallel to the vertical wires, was considered. This 2D simplification neglects the out-of-plane wire geometry, resulting in an overestimation of the effective porosity to 62%. To compensate for this discrepancy and maintain the target porosity of 38% in the 2D representation, the wire diameter was adjusted to 1.31 mm. The solid wall was modelled as a simple 2 m high structure with a uniform thickness of 4.5 cm. All surfaces within the computational domain, including the ground plane, were modelled as smooth surfaces with zero roughness.

The ambient air temperature was set to 35 °C to represent elevated summer temperatures. The corresponding air density and dynamic viscosity were set to 1.15 kg/m^3 and 1.88×10^{-5} kg/(m·s), respectively [50]. A range of free-stream velocities from 1 m/s to 50 m/s were simulated to encompass typical wildfire wind conditions. The initial computational domain dimensions were 120 m in length and 50 m in height for both the wall and fence configurations. However, subsequent analysis revealed that while this domain size was adequate for the permeable fence, it influenced the results for the impermeable wall. Consequently, the domain length and height for the solid wall simulations were extended to 300 m and 150 m, respectively. Further domain refinement in both cases yielded changes of less than 1% in the results.

The computational domain boundaries, permeable fence, and impermeable wall were modelled as no-slip walls, with the exception of the inlet and outlet. At the inlet, a uniform velocity profile was prescribed. As a consequence of viscous effects in the near-wall region and the application of a no-slip boundary condition at the ground plane, a boundary layer developed upstream of both the solid wall and porous fence configurations. This boundary layer exhibited a characteristic velocity profile, with zero velocity at the ground surface and a monotonic increase in velocity with increasing height. At the outlet, a zero-gradient boundary condition was imposed, allowing the solver to determine flow variables, and effectively minimizing boundary influence on the upstream flow field.

2.2. Computational Mesh Generation and Refinement

Appropriate mesh refinement is crucial to manage computational resources and avoid exceeding available memory. The initial mesh for the impermeable wall consisted of approximately 37,500 elements, predominantly quadrilateral elements, with element sizes of 1 mm and 2 mm near the wall and coarser elements further from the wall and ground (see Figure 1a). The porous fence was initially discretized using approximately 66,994 predominantly quadrilateral elements. The perimeter of each wire was divided into approximately 82 segments, with coarser elements employed away from the fence and ground (see Figure 1b). Adaptive mesh refinement was subsequently employed, focusing on regions exhibiting high residuals, primarily between the ground and a height of 6 m. This refinement process resulted in final mesh counts of 437,295 elements for the impermeable wall and 492,481 elements for the permeable fence. The final mesh distributions near critical regions are shown in Figure 2a,b for the impermeable wall and permeable fence, respectively.

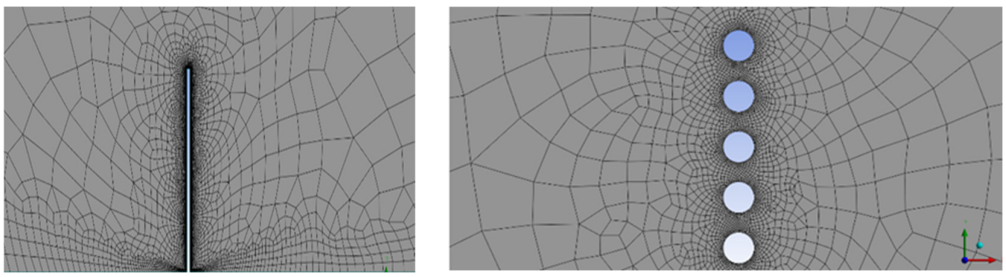

(**a**) (**b**)

Figure 1. Initial mesh configurations: (**a**) mesh around the solid wall; (**b**) mesh around the top wires of the porous fence (38% porosity).

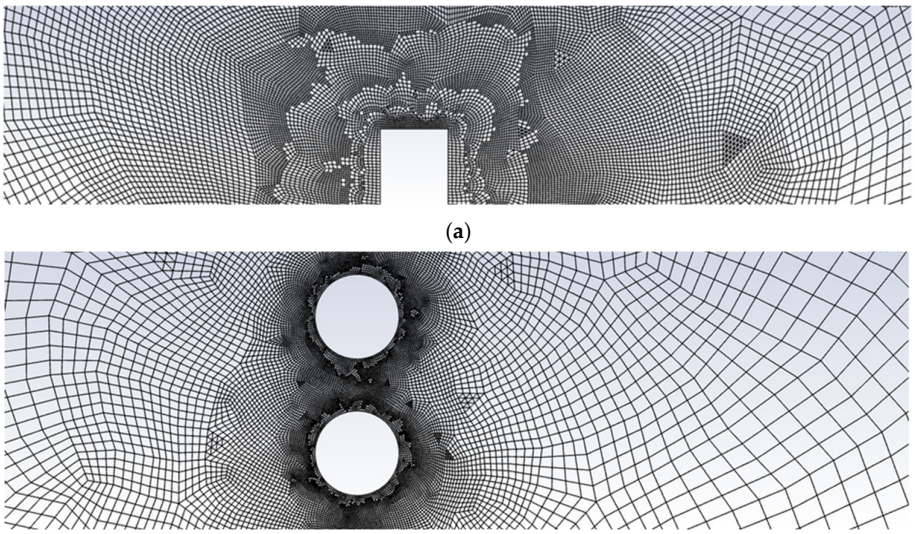

(**a**)

(**b**)

Figure 2. Final mesh configurations: (**a**) mesh around the top of the solid wall; (**b**) mesh around the top wires of the porous fence (38% porosity).

Initial mesh quality was assessed based on average element quality, aspect ratio, skewness, and orthogonality. For the impermeable wall mesh, the element quality was 0.82, the aspect ratio was 1.35, the skewness was 0.18, and the orthogonal quality was 0.96. For the permeable fence mesh, the corresponding values were 0.83 for element quality, 1.22 for aspect ratio, 0.19 for skewness, and 0.96 for orthogonal quality. According to ref. [51], these values indicate good mesh quality. In both cases, some elements initially exhibited suboptimal quality metrics. These were manually improved during the adaptation process. Additionally, the software's automatic mesh quality improvement functionality was utilized.

2.3. Numerical Solution Procedure

The computational fluid dynamics (CFD) simulations were performed using the Shear Stress Transport (SST) k− ω turbulence model. This two-equation Reynolds-Averaged Navier–Stokes (RANS) model accounts for turbulent effects and generally provides robust and reliable results [52]. Pressure–velocity coupling was achieved using the Rhie–Chow interpolation scheme. Solution convergence was monitored through the residuals of turbulent kinetic energy (k) and specific dissipation rate (ω), with under-relaxation factors set at 0.75. A second-order discretization scheme was employed for the spatial discretization of the governing equations.

2.4. Verification of Computational Results

The computational results require verification, and two criteria—residuals and the Grid Convergence Index (GCI)—were used for this purpose. All computational runs in this study achieved convergence, with residuals of less than 10^{-5}. All residuals were set to a maximum value of 10^{-5}. In practice, the continuity equation was the last to converge; upon its convergence, the residuals for velocity in the x and y directions, k, and ω were less than 10^{-7}. This level of convergence is considered acceptable for computational fluid dynamics [52].

The second criterion was the calculation of the GCI to ensure grid-independent results. The GCI was calculated using the formulas suggested by Roache [53] and others [54–56]. The procedure for the verification of modelling the wall at a wind speed of 10 m/s using three consecutive mesh refinements is detailed below and summarized in Table 1.

Table 1. Results of the grid refinement study for the 2 m porous fence at a free-stream velocity of 10 m/s, employed for Grid Convergence Index (GCI) calculation and solution verification.

Free Wind Speed (m/s)	Number of Elements	h_{max} (m) [1]
10 m/s	66,994	2.74076
10 m/s	367,120	2.90792
10 m/s	492,481	2.8227

[1]: h_{max} represents the maximum height of the lowest streamline passing over the porous fence.

Table 1 shows the number of meshes and the results of three consecutive wall models at a wind speed of 10 m/s. First, the grid refinement ratio, r, was calculated as follows [54]:

$$r = \left(\frac{\textit{the number of grids of the fine grid}}{\textit{the number of grids of the coarse grid}}\right)^{1/d} = \left(\frac{492,481}{66,994}\right)^{1/2} = 2.711295 \quad (1)$$

In the above equation, d represents the dimensionality [24], which is equal to 2 for the present two-dimensional model. Given the numerical solutions obtained on the course, medium, and fine grids, denoted as f_{coarse}, f_{medium}, and f_{fine}, respectively, the order of convergence (p) is determined as follows [54]:

$$p = \frac{Ln\left|(f_{coarse} - f_{medium})/(f_{medium} - f_{fine})\right|}{Ln\, r} = \frac{Ln|(2.74076 - 2.90792)/(2.90792 - 2.8227)|}{Ln\, 2.711295} = 0.673715 \quad (2)$$

The value of the relative error of two grids (e) in the simulations is calculated as follows [54]:

$$\epsilon = \frac{f_{coarse} - f_{fine}}{f_{fine}} = \frac{2.74076 - 2.8227}{2.8227} = -0.02903 \quad (3)$$

A safety factor (F_s) of 1.25 is typically employed when performing GCI analysis with three or more grid refinements. The GCI is then calculated using the following formula [54]:

$$GCI = F_s \frac{\epsilon}{r^p - 1} = 1.25 \frac{-0.02903}{2.711295^{0.673715} - 1} = -0.03787 \quad (4)$$

The calculated GCI is 3.8%, indicating good grid convergence, as values below 5% are typically considered acceptable in computational fluid dynamics.

3. Results

The numerical simulations, as detailed in previous sections, were performed at free-stream velocities of 1 m/s, 10 m/s, 20 m/s, and 50 m/s for both solid walls and the porous fence. The resulting flow fields are presented herein.

3.1. Characterization of Flow Around the Solid Wall

Figure 3a shows the flow field around a 2 m high wall at a free-stream velocity of 10 m/s. Figure 3b provides the velocity vectors in the region around the wall. The figures clearly demonstrate flow deflection well upstream of the wall, indicating the influence of the solid wall's presence on the approaching flow.

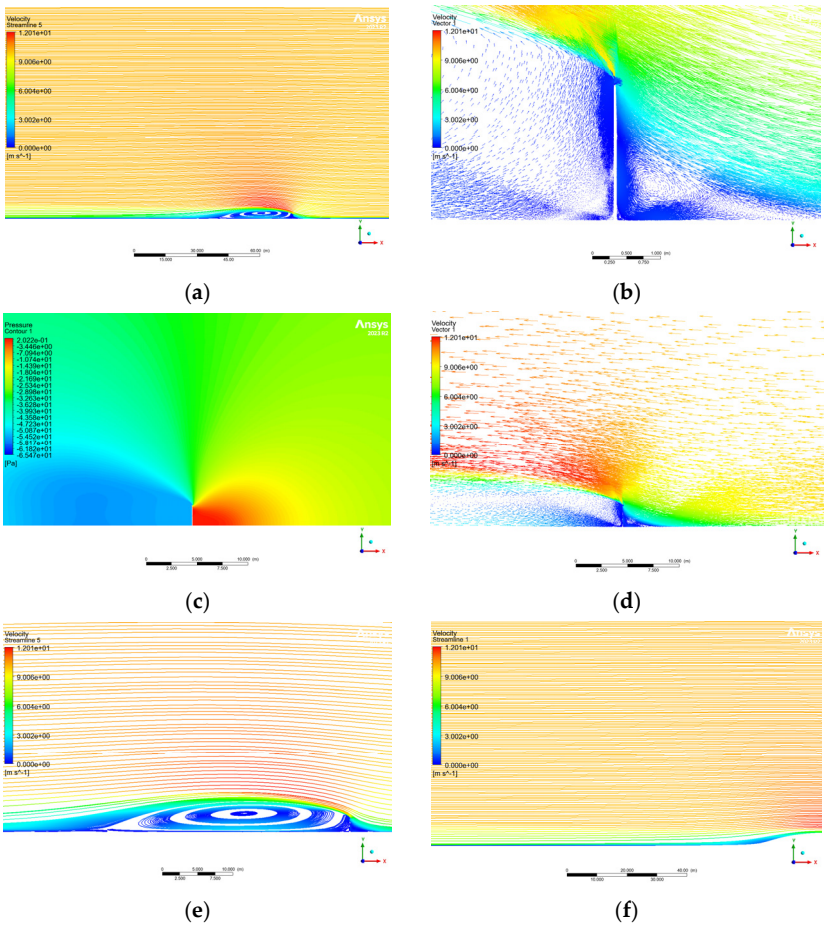

Figure 3. Flow around a 2 m high wall at a free-stream velocity of 10 m/s and 35 °C. (**a**) Streamlines within the computational domain; (**b**) velocity vectors near the wall; (**c**) pressure distribution showing high- and low-pressure regions; (**d**) magnified view of velocity vectors near the wall; (**e**) downstream streamlines showing vortex formation and downward trajectory; (**f**) streamlines returning to ground level.

A recirculation zone, characterized by a low-velocity vortex and flow reversal, forms at the upstream base of the wall (see Figure 3b). This recirculation region creates a localized high-pressure zone (see Figure 3c), effectively acting as a ramp and forcing the oncoming streamlines upward. Consequently, all approaching fluid is diverted over the wall.

Downstream of the wall, the flow continues its upward trajectory (see Figure 3a,d), generating a region of lower pressure on the downstream side of the wall due to flow separation and the formation of a large vortex (see Figure 3a,b,d). The lowest streamline to go over the wall reaches a maximum height (h_{max}) of 4.3 m at a downstream distance (X_{max}) of 14.5 m from the wall. Beyond X_{max} (see Figure 3e), the influence of the lower-pressure

region beneath the flow causes the flow to descend. The streamline returns to the initial wall height of 2 m at a distance of 30.8 m downstream from the wall. Further downstream (see Figure 3f), the flow continues its downward movement, reaching a height of 0.1 m at a distance (L_f) of 57 m. Beyond L_f, the flow re-establishes a predominantly horizontal trajectory until exiting the computational domain.

This general flow pattern, indicative of bluff body flow, is observed across all simulated free-stream velocities. The quantitative results for these variations are summarize in Table 2.

Table 2. Simulation results for flow over a 2 m high wall at 35 °C.

Wind Speed (m/s)	h_{max} [1] (m)	X_{max} [2] (m)	L_r [3] (m)	L_f [4] (m)
1	4.2	13.4	29.7	56.4
10	4.3	14.5	30.8	57.0
20	4.4	14.5	31.6	57.5
50	5.5	27	55.6	72.7

[1] h_{max}: the maximum height attained by the lowest streamline. [2] X_{max}: the downstream distance from the wall at which the lowest streamline reaches h_{max}. [3] L_r: the downstream distance from the wall at which the lowest streamline returns to the initial wall height of 2 m. [4] L_f: the downstream distance at which the lowest streamline reaches a height of 0.1 m from the ground.

Table 2 summarizes the computational results for flow over a 2 m high wall subjected to free-stream wind speeds ranging from 1 m/s to 50 m/s. The table details the trajectory of the lowest streamline of the 35 °C airflow as it passes over the wall.

Table 2 shows, at a wind speed of 1 m/s, the lowest streamline passing over the fence, reaching a maximum height (h_{max}) of 4.2 m at a downstream distance (X_{max}) of 13.4 m from the wall. Beyond X_{max}, the streamline descends, returning to the wall's height (2 m) at a distance (L_r) of 29.7 m downstream. Further downstream, the positive influence of the wall on the flow diminishes as the streamline continues its descent, approaching a height of 0.1 m at approximately 56.4 m downstream (L_f). It should be noted that a height of 0.1 m was selected to compare cases as the flow continued its decent with a very low angle, and selecting zero height for comparison does not appear to be the best choice. This indicates that the protective effect of the wall against airborne particles, such as firebrands, is significantly reduced beyond this distance (L_f), as the airflow is no longer effectively deflected upwards.

As the wind speed increases, the values of h_{max}, X_{max}, L_r, and L_f also increase. Specifically, at 50 m/s, these parameters reach values of 5.5 m, 27 m, 55.6 m, and 72.7 m, respectively. This demonstrates a clear correlation between increasing free-stream velocity and the extent of the flow's upward trajectory and subsequent downstream impact point.

3.2. Characterization of Flow Around the Porous Fence

Figure 4a illustrates the flow field around a fence with a porosity of 38% at a free-stream velocity of 10 m/s. Similarly to the solid wall case, the upstream flow is influenced by the presence of the porous fence, albeit to a lesser extent. Flow below a vertical height of 1.2 m at the domain inlet passes through the porous fence, while flow above this height bypasses (overtops) it (see Figure 4b). Notably, no significant flow reversal or large-scale vortex shedding is observed upstream of the fence (see Figure 4b). However, as shown in Figure 4c, a slight positive static pressure gradient develops upstream of the fence, accompanied by a corresponding negative static pressure gradient downstream. Figure 4d, a magnified view around two top wires, reveals localized pressure variations. A small region of elevated static pressure forms upstream of each wire, while a region of reduced static pressure is observed within the inter-wire spacing. In addition, the static pressure is also negative immediately downstream of each wire (see Figure 4d). The inter-wire

velocity reaches a maximum of approximately 21.3 m/s. Small-scale vortex shedding occurs downstream of each wire (see Figure 4e).

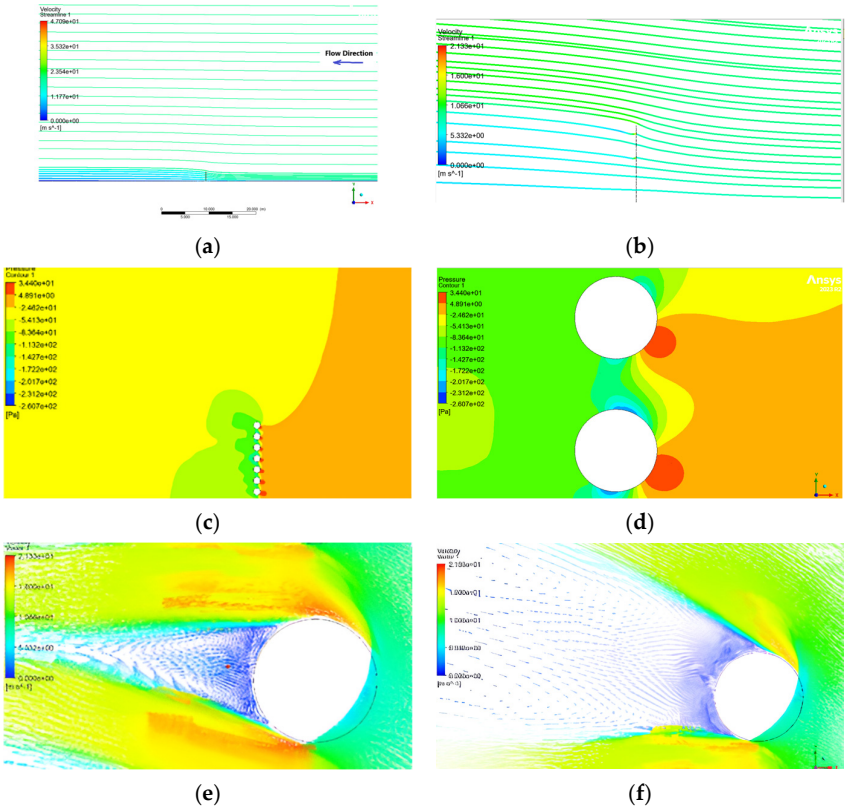

Figure 4. Flow around a 2 m high porous fence (38% porosity) at a free-stream velocity of 10 m/s and 35 °C. (**a**) Streamlines within the computational domain; (**b**) close-up view of streamlines near the fence; (**c**) pressure contours near the top wires; (**d**) magnified view of pressure variations around two top wires; (**e**) velocity vectors around a single wire; (**f**) velocity vectors near the topmost wires.

This flow pattern is consistent across all wires, with the exception of the topmost wire, which exhibits the most pronounced vortex (Figure 4f). This is attributed to the absence of flow above the topmost wire, unlike the other wires, which experience flow on both sides. The absence of downward momentum from above results in a larger recirculation zone and a lower-pressure region.

The lowest streamline that overtops the porous fence continues its upward trajectory (analogous to the flow over the solid wall) before eventually becoming horizontal. At a free-stream velocity of 10 m/s, this occurs at a downstream distance of 28.5 m, where the streamline reaches a height of 2.8 m. A key difference compared to the solid wall case is that the lowest streamline passing over the fence does not return to ground level, as the flow passing through the fence fills the region between the ground and this streamline. It was also observed that the downward momentum of the flow after reaching the maximum height becomes negligible as the free-stream wind speed increases. However, at low wind speeds, such downward movement can be observed (see Figure 5). The main reason for this different pattern can be explained by the percentage of the flow passing the fence. At a wind speed of 1 m/s, only 50% of streamlines pass through the fence, but this percentage increases at higher wind velocities. Therefore, more available space exists to divert the flow downward at lower free-stream velocities. Apart from the small-scale recirculation zones behind each wire, no significant upstream flow reversal is observed.

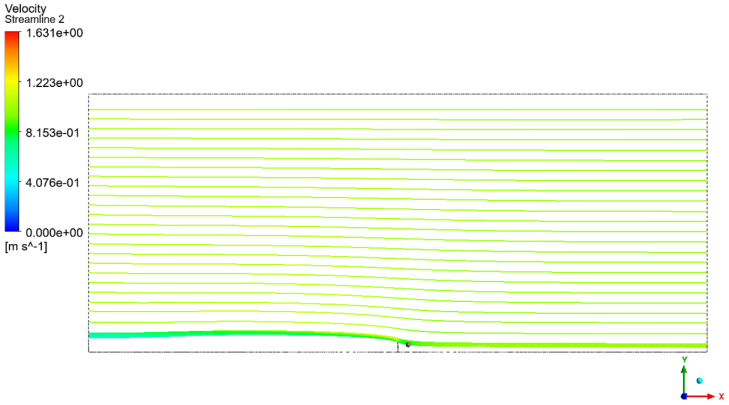

Figure 5. Streamline distribution around the fence with 38% porosity, subjected to a free-stream velocity of 1 m/s and an ambient air temperature of 35 °C.

The flow pattern around the porous fence remains qualitatively similar across all simulated free-stream velocities. Table 3 presents the results of CFD simulations conducted across a range of free-stream velocities from 1 m/s to 50 m/s. At a free-stream velocity of 1 m/s, streamlines originating below an inlet height (h_0) of 1.0 m are observed to permeate the fence. These streamlines exhibit an upward trajectory, with the streamline originating at h_0 = 1.0 m reaching a height of 2 m upon approaching the fence. Streamlines originating above this inlet height (1 m) bypass the fence.

Table 3. Results for the 2 m high, 38% porosity porous fence at varying free-stream velocities.

Wind Speed (m/s)	h_0 [1] (m)	h_{max} [2] (m)	X_{max} [3] (m)	h_f [4](m)
1	1.0	3.4	27.3	2.8
10	1.2	2.8	28.5	2.8
20	1.4	2.8	>60 m	2.8
50	1.5	2.6	>60 m	2.6

[1]: h_o represents the inlet height of the lowest streamline deflected over the fence. [2]: h_{max} denotes the maximum height of the lowest streamline deflected over the fence. [3]: X_{max} represents the downstream distance from the fence at which the lowest streamline deflected over the fence reaches its maximum height. [4]: h_f represents the outlet height of the lowest streamline deflected over the fence at the domain exit.

Streamlines interacting with the porous fence experience a localized acceleration and a corresponding reduction in static pressure within the mesh interstices (see Figure 4d,e). A recirculation zone with reduced pressure forms in the wake region downstream of the wires, characterized by small-scale vortex shedding with a characteristic length of the order of a few wire diameters (see Figure 4e). Downstream, these streamlines decelerate and are advected at reduced velocities.

At a free-stream velocity of 1.0 m/s, the maximum height (h_{max}) of the lowest streamline passing over the fence is 3.4 m, occurring at a downstream distance (X_{max}) of 27.3 m. Beyond X_{max}, the streamline descends slightly, reaching a height of 2.8 m at the domain outlet (see Figure 5).

As the free-stream velocity increases, a greater proportion of the flow has sufficient momentum to pass through the fence. At free-stream velocities of 10 m/s, 20 m/s, and 50 m/s, the corresponding inlet height (h_o) of the lowest transmitted streamline deflected over the fence increases to 1.2 m, 1.4 m, and 1.5 m, respectively. Concurrently, the thickness of the flow bypassing over the fence decreases. Due to the increased momentum of the free stream, which pushes the deflected streamlines down, h_{max} decreases, and X_{max} shifts further downstream. The computational results presented in Table 3 confirm this trend, showing a decrease in h_{max} with increasing wind speed. At 50 m/s, h_{max} reaches its

minimum value of 2.6 m. Table 3 also indicates that at lower wind speeds, X_{max} occurs closer to the fence, increasing with wind speed.

Furthermore, the results show that at lower wind speeds (up to 10 m/s), the lowest streamline exhibits a downward trajectory after reaching h_{max}. However, at higher wind speeds, this downward deflection is not observed; the streamline continues to ascend at a very small angle, with X_{max} occurring outside the computational domain. This absence of downward deflection is attributed to the increased flow transmission through the fence, reducing the available space for streamline deflection.

The outlet height (h_f) of the lowest streamline at the domain outflow boundary is influenced by both the maximum vertical height (h_{max}) and the streamline's trajectory downstream of X_{max}. At a free-stream velocity of 1 m/s, h_{max} is at its maximum, but the streamline exhibits the steepest downward trajectory, resulting in an h_f of 2.8 m. As the free-stream velocity increases to 10 m/s, h_{max} decreases; however, the reduced streamline slope and the decreased distance between X_{max} and the domain outflow boundary result in a negligible change in h_f. At a free-stream velocity of 20 m/s, where a substantial portion of the flow (70%) is transmitted through the fence, no downward deflection of the streamline is observed, and X_{max} exceeds the domain length (60 m). In this case, h_f remains at 2.8 m. At a free-stream velocity of 50 m/s, a similar lack of downward deflection is observed, with X_{max} again exceeding the domain length. However, due to the lower value of h_{max} compared to the 20 m/s case, h_f decreases to 2.6 m.

4. Discussion

The computational results presented in the preceding section were validated using a residual convergence criterion of 10^{-5} and the GCI. However, it is crucial to acknowledge the underlying assumptions and limitations of the model. The model employs a two-dimensional representation, while the physical scenario is inherently three-dimensional. The use of streamlines to represent firebrand trajectories is a simplification, particularly where streamlines exhibit steep angles. Due to their inertia, firebrands will not perfectly follow streamline paths. The model assumes constant and uniform temperature, which is not strictly valid due to the presence of glowing and flaming embers and their thermal influence on the surrounding environment. Heat transfer between the air and the ground, wall, and porous mesh was neglected. The model assumes constant pressure and density, which deviates from reality as altitude changes. The ground surface is modelled as smooth, neglecting the influence of vegetation and surface roughness. The model assumes a perfectly horizontal ground plane, which may not accurately represent real-world terrain. A steady and uniform wind speed profile is imposed at the computational domain inlet, neglecting potential variations in the approaching flow. However, a sufficient upstream distance was included to allow for boundary layer development at the ground plane. Despite these simplifications, consistent assumptions were applied to both the solid wall and porous fence cases. Consequently, the results are primarily intended for comparative analysis between these two scenarios and should be interpreted as indicative rather than quantitatively precise representations of real-world firebrand behaviour. It should be noted that a wide range of free-stream velocities (1–50 m/s) were considered, corresponding to Reynolds numbers (based on a characteristic length of 2 m) from 1.2×10^5 to 6.0×10^6. This range encompasses potential uncertainties arising from factors such as heat transfer, which was not modelled. For instance, an estimated 5 °C increase in the average air temperature at 20 m/s (from 35 °C) would result in a kinematic viscosity change from 1.64×10^{-5} m^2/s to 1.69×10^{-5} m^2/s [50], corresponding to a Reynolds number change from 2.44×10^6 to 2.37×10^6. This change is equivalent to a velocity shift of approximately 0.6 m/s (from 20 m/s to 19.43 m/s), well within the velocity range considered. Similarly, the impact

of this temperature change on h_{max} for a 2 m wall is estimated to be only 0.01 m (based on interpolation from Table 2). These analyses demonstrate that while the results are approximate, they capture the essential flow physics and are suitable for drawing valid conclusions regarding the relative performance of the wall and fence.

In the absence of field data, the validity of the present computational approach is partially established through comparison with the existing literature, encompassing both computational and wind tunnel experimental studies. For the solid wall configuration, the simulations accurately capture the fundamental fluid mechanics principle of a stagnation zone upstream and a low-pressure region with a prominent vortex and flow reversal immediately before the wall [50]. While previous research has primarily focused on drag force calculations [57,58], often at lower Reynolds numbers due to differing length scales, the current study provides novel insights into the downstream flow field, including flow reattachment and maximum streamline height, at significantly higher Reynolds numbers relevant to wildfire conditions. Similarly, while previous studies have characterized the flow around individual wires in porous fences [10,59], observing stagnation zones and wake formation, this study extends the analysis to the flow field downstream of the entire fence structure. Experimental observations [41] of firebrand trapping and wandering within these wakes provide further qualitative support for the present findings. By independently confirming the existence of these wakes and associated low-pressure regions, this work contributes a more comprehensive understanding of the flow dynamics relevant to firebrand mitigation by solid walls and porous fences.

Solid walls demonstrate effective flow deflection capabilities. A 2 m wall deflects the incident flow upwards, achieving maximum vertical displacements ranging from 4.2 m to 5.5 m at free-stream velocities of 1 m/s and 50 m/s, respectively. The peak height of the lowest streamline reaches distances of 13.4 m and 27 m downstream of the wall at these corresponding velocities. However, beyond these points of maximum height, the flow descends, returning to the wall's height of 2 m at downstream distances of approximately 29.7 m (1 m/s) and 55.6 m (50 m/s). Beyond these points, the wall offers negligible protection. Two practical considerations are paramount. First, during bushfire events, wind speeds are inherently unsteady and turbulent. Therefore, positioning buildings in close proximity to the wall is crucial to maximize its protective effectiveness. Second, due to the inherent inertia of firebrands, they may deviate from the predicted flow path and directly impact the wall, especially those approaching the wall along low-elevation streamlines and experiencing steep angles to pass the wall. Consequently, while buildings located at the reattachment length (L_r) remain susceptible to firebrand impingement, the firebrand flux intensity is reduced. In summary, solid walls provide substantial protection against firebrand attacks in close proximity; however, their effectiveness diminishes significantly with increasing downstream distance.

The 38% porosity fence also demonstrates effective firebrand mitigation. Low-trajectory firebrands are transmitted through the mesh, undergoing filtration. The existing literature suggests that penetration is limited to small firebrands, significantly reducing the ignition probability compared to larger embers, with a risk reduction exceeding 90% within a downstream distance of approximately 2 m [41].

The results demonstrate that the proportion of flow filtered by the porous fence increases with increasing free-stream velocity. For instance, at 1 m/s, approximately 50% (1/2, see Table 3) of firebrands are filtered, increasing to 75% (1.5/2, see Table 3) at a velocity of 50 m/s. This estimation assumes a uniform firebrand flux intensity across different elevations.

Similarly to solid walls, the porous fence deflects a portion of the flow upwards, albeit to a lesser degree. High-trajectory firebrands are diverted over the fence, reaching

maximum heights of 3.4 m at 1 m/s and 2.6 m at 50 m/s. Notably, at higher wind speeds, this deflected flow does not descend significantly; at 1 m/s, the descent is only 0.6 m (=3.4 − 2.8, see Table 3). This limited descent suggests that the porous fence provides extended downwind protection.

In summary, the porous fence offers good (though not absolute) protection in close proximity, with effectiveness increasing with downstream distance as smaller transmitted embers are extinguished.

Comparing the porous fence and solid walls, the walls provide greater deflection of high-trajectory firebrands. For example, at 1 m/s, the maximum protected heights for walls and the porous fence are 4.2 m and 3.4 m, respectively. At 50 m/s, these corresponding heights are 5.5 m and 2.6 m. This limitation of the fence can be addressed by increasing its height.

A low-porosity fence was selected for this study. It is anticipated that as porosity increases, a greater proportion of the incident flow will pass through the fence and induce less flow deflection. Consequently, h_{max} is expected to decrease, approaching a minimum value equal to the fence height (2 m), while a larger proportion of firebrands would be filtered. Furthermore, the reduced or negligible downward flow deflection is expected to enhance the fence's protective range against low-flying firebrands.

It should be noted that this study focuses solely on firebrand transport; however, other factors are also critical for infrastructure protection during wildfires. A significant factor is radiant heat flux. In the event of a fire in close proximity to the barrier, a solid wall will effectively block the transmission of radiant heat. While previous research indicates that porous fences can also block a considerable portion of radiant heat flux [60], even double-layered fences cannot provide complete protection in the near-field [61]. Furthermore, studies have shown that air temperatures immediately downstream of metal mesh fences can increase significantly and create tiny hot spots [62]. Therefore, it is prudent to ensure the absence of combustible vegetation in the near-wake region downstream of a porous fence if fuel sources are present upstream.

Previous investigations of drag force on porous fences have typically employed wind tunnel experiments [39] or simplified the analysis by assuming normal incidence of the approaching flow [10]. However, this study demonstrates that the assumption of normal flow incidence is not universally valid, particularly near the fence crest and for low-porosity fences. Consequently, this flow deflection should be considered in future calculations of both the magnitude and direction of the drag force. This study did not focus on quantifying drag forces, which remains a subject for future research.

5. Summary

The performance of a 2 m high solid wall and a 2 m porous fence (38% porosity and 2.11 cell size) in protecting buildings and structures from windblown ember attacks during bushfires was computationally investigated. Recognizing that wildfire conditions vary significantly, and no single scenario can represent all events, a representative scenario was selected for comparative analysis between the solid wall and porous fence. Several simplifying assumptions were also employed to facilitate the computational analysis.

The computational results demonstrate that both the solid wall and the porous fence offer effective protection. Solid walls are particularly effective at short distances, providing protection for structures up to heights of 4.2 m at a free-stream velocity of 1 m/s and 5.5 m at 50 m/s. The protective benefit of solid walls diminishes at downstream distances of 29.7 m (1 m/s) and 55.6 m (50 m/s), effectively ceasing beyond 56.4 m (1 m/s) and 72.7 m (50 m/s). Thus, solid walls are most effective when positioned close to the protected

structures, providing protection within a range of approximately 30 m to 70 m depending on the maximum wind speed.

The porous fence also exhibits substantial protective capabilities. Similarly to solid walls, it deflects embers to higher elevations, although to a lesser extent, protecting structures up to heights of 3.4 m (1 m/s) and 2.6 m (50 m/s). This protection extends over a considerable downstream distance. Furthermore, the porous fence provides effective near-field protection by filtering low and large flying embers. The small embers that penetrate the mesh have a significantly reduced probability of ignition within a short distance (a few metres) and are likely to be extinguished as they are advected further downstream. Increasing the height of the porous fence beyond 2 m is expected to provide protection for taller structures and extend the protected zone further downwind.

The findings of this study reveal that both solid walls and porous fences can provide effective mitigation of firebrand transport, although their protective mechanisms differ significantly. The practical implications of these findings suggest that solid walls offer good protection when the barrier can be located in close proximity to the structure being protected, typically within a distance of a few metres. However, when close proximity is not achievable, or when the objective is to provide protection to a series of structures lo-cated behind one another, porous fences represent a more advantageous solution. These findings align with established principles of flow modification for protection, as seen in various applications such as windbreaks or tress protecting crops and buildings, ice-breakers shielding bridge piers, groynes mitigating coastal erosion, bluff bodies to protect sensitive sensors from high-velocity flow, and drafting in cycling and motorsports.

Funding: This research received no external funding.

Institutional Review Board Statement: Not applicable.

Informed Consent Statement: Not applicable.

Data Availability Statement: The data presented in this study are available on request from the corresponding author.

Conflicts of Interest: The author declares no conflicts of interest.

References

1. Standards Australia. Construction of Buildings in Bushfire Prone Areas AS 3959:2018. SAI Global. Available online: https://infostore.saiglobal.com/en-au/search/standard/?searchTerm=AS%203959:2018&productFamily=STANDARD&q=AS%203959:2018 (accessed on 28 May 2022).
2. Deck, P. UL790 Standard Test Methods for Fire Tests of Roof Coverings. 2005. Available online: http://yiqi-oss.oss-cn-hangzhou.aliyuncs.com/aliyun/900101567/technical_file/file_132012.pdf (accessed on 28 May 2022).
3. Wadhwani, R.; Sullivan, C.; Wickramasinghe, A.; Kyng, M.; Khan, N.; Moinuddin, K. A review of firebrand studies on generation and transport. *Fire Saf. J.* **2022**, *134*, 103674. [CrossRef]
4. Babrauskas, V. Firebrands and embers. In *Encyclopedia of Wildfires and Wildland-Urban Interface (WUI) Fires*; Springer: Berlin/Heidelberg, Germany, 2020; pp. 431–444.
5. Cruz, M.G.; Sullivan, A.L.; Gould, J.S.; Sims, N.C.; Bannister, A.J.; Hollis, J.J.; Hurley, R.J. Anatomy of a catastrophic wildfire: The Black Saturday Kilmore East fire in Victoria, Australia. *For. Ecol. Manag.* **2012**, *284*, 269–285. [CrossRef]
6. Franklin, R. *Inferno: The Day Victoria Burned*; Slattery Media Group: Richmond, VIC, Australia, 2010.
7. O'Neill, S.J.; Handmer, J. Responding to bushfire risk: The need for transformative adaptation. *Environ. Res. Lett.* **2012**, *7*, 014018. [CrossRef]
8. Bushfire Warning Systems in Australia. Doctoral Dissertation, Worcester Polytechnic Institute, Worcester, MA, USA, 2010.
9. Suzuki, S.; Manzello, S.L. Experimental investigation of firebrand accumulation zones in front of obstacles. *Fire Saf. J.* **2017**, *94*, 1–7. [CrossRef]
10. Sharifian, A.; Buttsworth, D.R. Computational simulation of the wind-force on metal meshes. In Proceedings of the 16th Australasian Fluid Mechanics Conference (AFMC 2007), Gold Coast, Australia, 3–7 December 2007.
11. Koo, J.K.; James, D.F. Fluid flow around and through a screen. *J. Fluid Mech.* **1973**, *60*, 513–538. [CrossRef]

12. Amaki, K.; Hasegawa, T.; Narumi, T. Drag reduction in the flow of aqueous solutions of detergent through mesh screens. *Nihon Reoroji Gakkaishi* **2008**, *36*, 125–131. [CrossRef]
13. Armour, J.C.; Cannon, J.N. Fluid flow through woven screens. *AIChE J.* **1968**, *14*, 415–420. [CrossRef]
14. Schubauer, G.B.; Spangenberg, W.G.; Klebanoff, P.S. Aerodynamic Characteristics of Damping Screens. No. NACA-TN-2001, 1950.
15. Venkateshan, D.G.; Amrei, M.M.; Hemeda, A.A.; Cullingsworth, Z.; Corbett, J.; Tafreshi, H.V. Failure pressures and drag reduction benefits of superhydrophobic wire screens. *Colloids Surf. A Physicochem. Eng. Asp.* **2016**, *511*, 247–254. [CrossRef]
16. Baines, W.D.; Peterson, E.G. An investigation of flow through screens. *Trans. Am. Soc. Mech. Eng.* **1951**, *73*, 467–477. [CrossRef]
17. Ramon, G.Z.; Hoek, E.M. On the enhanced drag force induced by permeation through a filtration membrane. *J. Membr. Sci.* **2012**, *392*, 1–8. [CrossRef]
18. Li, H.; Li, Y.; Gao, F.; Zhao, Z.; Xu, L. CFD–DEM simulation of material motion in air-and-screen cleaning device. *Comput. Electron. Agric.* **2012**, *88*, 111–119. [CrossRef]
19. Ozkan, G.M.; Firat, E.; Akilli, H. Control of vortex shedding using a screen attached on the separation point of a circular cylinder and its effect on drag. *J. Fluids Eng.* **2017**, *139*, 071107. [CrossRef]
20. Kirsh, V.A. The viscous drag of three-dimensional model fibrous filters. *Colloid J.* **2006**, *68*, 261–266. [CrossRef]
21. San Andrés, L.; Chirathadam, T.A.; Ryu, K.; Kim, T.H. Measurements of drag torque, lift-off journal speed, and temperature in a metal mesh foil bearing. *J. Eng. Gas Turbines Power* **2010**, *132*, 112503. [CrossRef]
22. Tsukrov, I.; Drach, A.; DeCew, J.; Swift, M.R.; Celikkol, B. Characterization of geometry and normal drag coefficients of copper nets. *Ocean. Eng.* **2011**, *38*, 1979–1988. [CrossRef]
23. Lee, Y.B.; Kim, C.H.; Kim, T.H.; Kim, T.Y. Effects of mesh density on static load performance of metal mesh gas foil bearings. *J. Eng. Gas Turbines Power* **2012**, *134*, 012502. [CrossRef]
24. Feng, K.; Zhao, X.; Zhang, Z.; Zhang, T. Numerical and compact model of metal mesh foil bearings. *Tribol. Trans.* **2016**, *59*, 480–490. [CrossRef]
25. San Andrés, L.; Abraham Chirathadam, T. A metal mesh foil bearing and a bump-type foil bearing: Comparison of performance for two similar size gas bearings. *J. Eng. Gas Turbines Power* **2012**, *134*, 102501. [CrossRef]
26. Park, S.H.; Seo, D.H.; Jeong, J.H. Experimental and numerical analysis of thermal flow in open-cell porous metal during Darcy-Forchheimer transition regime. *Appl. Therm. Eng.* **2020**, *181*, 116029. [CrossRef]
27. Robertson, A.F. Air porosity of open-weave fabrics* part I: Metallic meshes. *Text. Res. J.* **1950**, *20*, 838–844. [CrossRef]
28. Yang, G.; Xu, R.; Wang, Y.; Zhu, Y.; Ren, F.; Li, C.; Wu, J. Pore-scale numerical simulations of flow and convective heat transfer in a porous woven metal mesh. *Chem. Eng. Sci.* **2022**, *256*, 117696. [CrossRef]
29. Oun, H.; Kennedy, A. Experimental investigation of pressure-drop characteristics across multi-layer porous metal structures. *J. Porous Mater.* **2014**, *21*, 1133–1141. [CrossRef]
30. Dukhan, N.; Patel, P. Equivalent particle diameter and length scale for pressure drop in porous metals. *Exp. Therm. Fluid Sci.* **2008**, *32*, 1059–1067. [CrossRef]
31. Suleiman, A.S.; Dukhan, N. Long-domain simulation of flow in open-cell mesoporous metal foam and direct comparison to experiment. *Microporous Mesoporous Mater.* **2014**, *196*, 104–114. [CrossRef]
32. Jia, X.; Yang, J.; Lin, M.; Wang, Q. Pore scale analysis for flow and thermal characteristics in metallic woven mesh. *Int. J. Heat Mass Transfer.* **2024**, *218*, 124740. [CrossRef]
33. Iasiello, M.; Cunsolo, S.; Oliviero, M.; Harris, W.M.; Bianco, N.; Chiu, W.K.; Naso, V. Numerical analysis of heat transfer and pressure drop in metal foams for different morphological models. *J. Heat Transfer.* **2014**, *136*, 112601. [CrossRef]
34. Tao, S.; He, Q.; Yang, X.; Luo, J.; Zhao, X. Numerical study on the drag and flow characteristics of porous particles at intermediate Reynolds numbers. *Math. Comput. Simul.* **2022**, *202(C)*, 273–294. [CrossRef]
35. Hossain, M.S.; Shabani, B. Air flow through confined metal foam passage: Experimental investigation and mathematical modelling. *Exp. Therm. Fluid Sci.* **2018**, *99*, 13–25. [CrossRef]
36. Shapovalov, V. Porous metals. *MRS Bull.* **1994**, *19*, 24–28. [CrossRef]
37. Manzello, S.L.; Shields, J.R.; Yang, J.C.; Hayashi, Y.; Nii, D. On the use of a firebrand generator to investigate the ignition of structures in wildland-urban interface (WUI) fires. In Proceedings of the 11th International Conference on Fire Science and Engineering (INTERFLAM), London, UK, 3–5 September 2007; Interscience Communications Ltd.: London, UK, 2007.
38. Manzello, S.L.; Hayashi, Y.; Yoneki, Y.; Yamamoto, Y. Quantifying the vulnerabilities of ceramic tile roofing assemblies to ignition during a firebrand attack. *Fire Saf. J.* **2010**, *45*, 35–43. [CrossRef]
39. Sharifian, A.; Hashempour, J. A novel ember shower simulator for assessing performance of low porosity screens at high wind speeds against firebrand attacks. *J. Fire Sci.* **2016**, *34*, 335–355. [CrossRef]
40. Sharifian, A.; Hashempour, J. Wind tunnel experiments on effects of woven wire screens and buffer zones in mitigating risks associated with firebrand showers. *Aust. J. Mech. Eng.* **2020**, *18*, 156–168. [CrossRef]

41. Sharifian Barforoush, A.; Du Preez, M. Quantifying the effectiveness of a mesh in mitigating burning capabilities of firebrand shower. *Fire* **2022**, *5*, 150. [CrossRef]
42. Hashempour, J.; Sharifian, A. Effective factors on the performance of woven wire screens against leaf firebrand attacks. *J. Fire Sci.* **2017**, *35*, 303–316. [CrossRef]
43. Sharifian, A.; Wells, K. Performance assessment of ISO-5167 and symmetrical Venturi meters for measuring low Reynolds number turbulent incompressible isothermal flow. *Int. J. Thermofluids* **2024**, *22*, 100598. [CrossRef]
44. Zhang, H.Q.; Fey, U.; Noack, B.R.; König, M.; Eckelmann, H. On the transition of the cylinder wake. *Phys. Fluids* **1995**, *7*, 779–794. [CrossRef]
45. Wissink, J.G.; Rodi, W. Numerical study of the near wake of a circular cylinder. *Int. J. Heat Fluid Flow* **2008**, *29*, 1060–1070. [CrossRef]
46. Behara, S.; Mittal, S. Wake transition in flow past a circular cylinder. *Phys. Fluids* **2010**, *22*, 114104. [CrossRef]
47. Bloor, M.S. The transition to turbulence in the wake of a circular cylinder. *J. Fluid Mech.* **1964**, *19*, 290–304. [CrossRef]
48. Manzello, S.L.; Cleary, T.G.; Shields, J.R.; Maranghides, A.; Mell, W.; Yang, J.C. Experimental investigation of firebrands: Generation and ignition of fuel beds. *Fire Saf. J.* **2008**, *43*, 226–233. [CrossRef]
49. Koo, E.; Linn, R.R.; Pagni, P.J.; Edminster, C.B. Modelling firebrand transport in wildfires using HIGRAD/FIRETEC. *Int. J. Wildland Fire* **2012**, *21*, 396–417. [CrossRef]
50. Fox, R.W.; McDonald, A.T.; Pritchard, P.J. *Introduction to Fluid Mechanics*, 7th ed.; John Wiley & Sons: Hoboken, NJ, USA, 2009.
51. Sherrard, R. Ansys Fluent—Tips, Tricks, and Troubleshooting, Nimbix Supercomputing Suite 2020. Available online: https://support.nimbix.net/hc/en-us/articles/360044738671-ANSYS-Fluent (accessed on 10 April 2023).
52. ANSYS. *ANSYS Fluent Theory Guide 15.0*; ANSYS: Canonsburg, PA, USA, 2013; p. 33.
53. Roache, P.J. Perspective: A method for uniform reporting of grid refinement studies. *J. Fluids Eng.* **1994**, *116*, 405–413. [CrossRef]
54. Lee, M.; Park, G.; Park, C.; Kim, C. Improvement of grid independence test for computational fluid dynamics model of building based on grid resolution. *Adv. Civ. Eng.* **2020**, *2020*, 8827936. [CrossRef]
55. Malvoni, M.; Baglivo, C.; Congedo, P.M.; Laforgia, D. CFD modeling to evaluate the thermal performances of window frames in accordance with the ISO 10077. *Energy* **2016**, *111*, 430–438. [CrossRef]
56. Baker, N.; Kelly, G.; O'Sullivan, P.D. A grid convergence index study of mesh style effect on the accuracy of the numerical results for an indoor airflow profile. *Int. J. Vent.* **2020**, *19*, 300–314. [CrossRef]
57. Yakhot, A.; Liu, H.; Nikitin, N. Turbulent flow around a wall-mounted cube: A direct numerical simulation. *Int. J. Heat Fluid Flow* **2006**, *27*, 994–1009. [CrossRef]
58. Son, J.S.; Hanratty, T.J. Velocity gradients at the wall for flow around a cylinder at Reynolds numbers from 5 × 103 to 105. *J. Fluid Mech.* **1969**, *35*, 353–368. [CrossRef]
59. Zhu, J.; Holmedal, L.E.; Myrhaug, D.; Wang, H. Near-wall effect on flow around an elliptic cylinder translating above a plane wall. *Phys. Fluids* **2020**, *32*, 093607. [CrossRef]
60. Hashempour, J.; Sharifian, A.; Billingsley, J. Experimental measurement of direct thermal radiation through single-layer square-cell plain woven screens. *J. Heat Transf.* **2016**, *138*, 012701. [CrossRef]
61. Sharifian, A.; Buttsworth, D. Double-layered metal mesh screens to contain or exclude thermal radiation from bush fires. *J. Fire Prot. Eng.* **2010**, *20*, 291–311. [CrossRef]
62. Sharifian, A.; Buttsworth, D. Minimum safe standoff distance for protection from bushfire radiation by commercial metal meshes. In Proceedings of the 8th Australasian Heat and Mass Transfer Conference, Perth, Australia, 25–29 July 2005; Begel House Inc.: Danbury, CT, USA, 2005.